

High-Resolution Sensing in Communication-Centric ISAC: Deep Learning and Parametric Methods

Salmane Naoumi, Ahmad Bazzi, Roberto Bomfin, Marwa Chafii

Abstract—This paper introduces two novel algorithms designed to address the challenge of super-resolution sensing parameter estimation in bistatic configurations within communication-centric integrated sensing and communication (ISAC) systems. Our approach leverages the estimated channel state information derived from reference symbols originally intended for communication to achieve super-resolution sensing parameter estimation. The first algorithm, IFFT-C2VNN, employs complex-valued convolutional neural networks to estimate the parameters of different targets, achieving significant reductions in computational complexity compared to traditional methods. The second algorithm, PARAMING, utilizes a parametric method that capitalizes on the knowledge of the system model, including the transmit and receive array geometries, to extract the sensing parameters accurately. Through a comprehensive performance analysis, we demonstrate the effectiveness and robustness of both algorithms across a range of signal-to-noise ratios, underscoring their applicability in realistic ISAC scenarios.

Index Terms—Integrated sensing and communication (ISAC), bistatic radar, complex-valued neural network (CVNN), deep learning (DL), time of arrival (ToA) estimation, angle of arrival/departure (AoA/AoD) estimation.

I. INTRODUCTION

Integrated sensing and communication (ISAC) has been identified as a foundational technology expected to shape the future of 6G wireless systems [1]. This emerging paradigm enables the joint integration of radar sensing and communication functionalities within a unified framework, thereby enhancing spectrum efficiency and reducing both hardware and computational costs [2]. Such advancements open transformative possibilities across a wide range of applications, including automotive technology, Internet of things (IoT) [3], and robotics [4].

The ISAC framework can be classified into three primary areas of research: communication-centric, radar-centric, and joint design [5], [6]. In radar-centric approaches, communication data is embedded within radar waveforms [7], whereas

joint design methods focus on the co-optimization of sensing and communication systems, balancing these functionalities to meet application-specific requirements [8]. Recently, communication-centric ISAC has emerged as an effective approach to augment existing communication infrastructure with sensing capabilities. This approach leverages transmitted communication waveforms to extract sensing parameters, such as range and velocity, of targets within the environment. Studies have demonstrated the efficacy of communication waveforms for sensing, particularly in configurations such as mono-static ISAC systems that employ orthogonal time frequency space (OTFS) modulation [9] and time-division duplexing (TDD) massive multiple-input, multiple-output (MIMO) systems [10]. Among communication-centric configurations, the bistatic setting has gained recognition as one of the most practical solutions. By employing separate transmit and receive antennas, the bistatic configuration integrates seamlessly with existing communication infrastructures while expanding sensing coverage and minimizing interference [11]. Extensive research on bistatic radar systems has shown their effectiveness in estimating environmental sensing parameters by repurposing the channel state information (CSI) estimation process [12], [13]. Furthermore, recent studies have demonstrated the suitability of orthogonal frequency-division multiplexing (OFDM)-based waveforms in bistatic ISAC setups, further underscoring the feasibility of this configuration for practical implementations [14], [15].

A key challenge in bistatic ISAC systems is achieving super-resolution estimation of sensing parameters such as directions of departure and arrival, time of flight, and Doppler shifts. Super-resolution is crucial for attaining the sub-meter localization accuracy anticipated in 6G networks, which is necessary to support applications requiring high precision [16]. However, while super-resolution techniques significantly improve the estimation accuracy, they introduce considerable computational complexity. These methods often depend on advanced signal processing techniques that exceed the resolution limits of conventional approaches by fitting complex data models to measurements. Consequently, such techniques entail substantial computational demands, posing significant challenges for real-time implementation in resource-constrained environments [17]. Additionally, the accuracy of these methods often relies on the granularity of the parameter space search, further exacerbating their computational requirements.

To address some of these computational challenges, subspace-based approaches, such as multiple signal classifi-

This work is supported in part by the NYUAD Center for Artificial Intelligence and Robotics, funded by Tamkeen under the Research Institute Award CG010.

Salmane Naoumi is with NYU Tandon School of Engineering, Brooklyn, 11201, NY (e-mail: sn3397@nyu.edu).

Roberto Bomfin is with the Engineering Division, New York University (NYU) Abu Dhabi, UAE.

Ahmad Bazzi and Marwa Chafii are with the Engineering Division, New York University (NYU) Abu Dhabi, UAE and NYU WIRELESS, NYU Tandon School of Engineering, Brooklyn, NY.

Manuscript received xxx

cation (MUSIC) and estimation of signal parameters via rotational invariant techniques (ESPRIT), offer a partial solution by leveraging signal and noise subspaces for parameter estimation, thereby reducing the required computational load [18], [19]. However, these methods require a large number of continuous samples and may experience performance degradation in low-signal-to-noise ratio (SNR) scenarios or with closely spaced scatterers. Alternatively, compressive sensing (CS) techniques present another promising approach by formulating the sensing problem as a sparse signal recovery task. By exploiting signal sparsity across spatial, temporal, and frequency domains, CS can achieve super-resolution with fewer measurements [20]. However, as CS-based algorithms extend to higher-dimensional estimation, their computational complexity increases substantially, and the need for a large number of measurements becomes restrictive in environments with short channel coherence times and limited antenna arrays [21].

On another front, recent advances in machine learning (ML), particularly deep learning (DL), have shown promise for computationally efficient super-resolution parameter estimation by offering adaptability to complex environments and computational flexibility [22], [23]. Neural network (NN)-based methods have increasingly attracted attention in radar signal processing applications, where they provide notable advantages over traditional techniques, including enhanced super-resolution capabilities and improved generalization across varying system configurations and imperfections [24]. In the ISAC context, DL has proven effective in vehicular network ISAC scenarios [25], while recent works have proposed DL techniques for dual estimation tasks in uplink ISAC OFDM systems [26]. To the best of our knowledge, however, the specific problem of sensing parameter estimation in bistatic ISAC systems using DL methods has yet to be thoroughly explored in the literature.

In this paper, we address this gap by proposing a novel DL-based model for joint sensing parameter estimation in bistatic communication-centric ISAC setups. Specifically, we focus on the estimation of angle of arrival (AoA), angle of departure (AoD), and time of arrival (ToA) parameters. In addition, we propose a parametric method that leverages the system characteristics as well as the structure of the estimated channel matrix to estimate the sensing parameters. Both methods aim to achieve high estimation accuracy while significantly reducing computational complexity, thus enabling real-time applications within next-generation wireless systems.

In summary, our work makes the following key contributions

- We introduce *IFFT-convolutional complex-valued neural network (C2VNN)*, a specialized DL architecture tailored for high-resolution estimation of sensing parameters. The proposed method leverages coarse estimates obtained from the inverse fast Fourier transform (IFFT) of the estimated channel matrix to focus computational resources on regions of interest around target peaks in the transformed domain. This preprocessing enables IFFT-C2VNN to efficiently capture the fine-grained details necessary for

precise parameter estimation. The model architecture integrates complex-valued convolutional layers and enhances the estimation precision with minimal computational overhead. Training is performed using simulation data under varying SNR conditions, with mean squared error (MSE) employed as the training loss function.

- We propose *PARAMING*, a PARAMetric method for joint angles and tiMING estimation that exploits the full space-time structure of the system model. More precisely, PARAMING restructures the estimated CSI into compact sub-array matrices, making full use of array geometry, as well as OFDM structure. A truncated singular value decomposition (SVD) is then applied to isolate the principal components of the transformed matrix, enabling accurate ToA estimation for each target/clutter component without requiring a grid search. Subsequently, a two-stage least squares (LS) fitting process followed by 2D regression is applied to jointly compute the AoA and AoD estimates for each ToA value, thereby providing fine-grained spatial and temporal super-resolution. As a result, PARAMING provides 3D sensing (AoA, AoD and ToA) information for each target and clutter component with low complexity and high resolution, by leveraging model-based transformations.
- We present a comprehensive computational complexity analysis of PARAMING and IFFT-C2VNN, quantifying the required multiplications and additions for each method. Additionally, we compare the proposed methods to the conventional maximum likelihood estimator (MLE) approach, highlighting their significant computational advantages, particularly for real-time processing and high-resolution sensing tasks.
- We conduct a comprehensive evaluation of the proposed PARAMING and IFFT-C2VNN methods for estimating key sensing parameters, comparing their performance against state-of-the-art methods. The results demonstrate the superior estimation accuracy and robustness of the proposed methods across varying SNR levels. Furthermore, we show that both methods achieve significantly lower latency compared to grid-based approaches, making them highly efficient for real-time ISAC applications. Additionally, we extend the proposed methods to include Doppler frequency estimation, demonstrating their adaptability and strong performance in scenarios with moving targets.

Notation: Upper-case and lower-case boldface letters denote matrices and vectors, resp. $(\cdot)^T$, $(\cdot)^*$ and $(\cdot)^H$ represent the transpose, the conjugate and the transpose-conjugate operators. We denote by $*$ the convolution operator. For any complex number $z \in \mathbb{C}$, the real part of z is denoted as $\Re(z)$, whereas the imaginary part is denoted as $\Im(z)$. The ℓ_2 norm of a vector \mathbf{x} is denoted as $\|\mathbf{x}\|$. The matrices \mathbf{F} and \mathbf{I} are the Fourier and the identity matrices with appropriate dimensions, resp. For matrix indexing, the $(i, j)^{th}$ entry of matrix \mathbf{A} is denoted by $[\mathbf{A}]_{[i,j]}$ and its j^{th} column is denoted as $\mathbf{A}_{[:,j]}$. The operator \otimes is the *Kronecker* product. The big- \mathcal{O} notation is $\mathcal{O}(\cdot)$. For a set

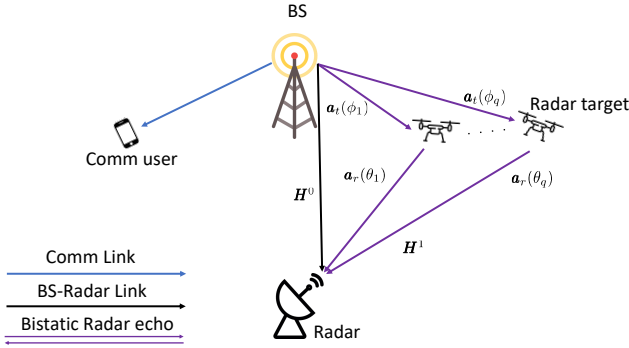


Fig. 1: Illustration of the bistatic communication-centric ISAC system model, where downlink transmissions from a base station (BS) to communication users serve as simultaneous illumination sources for radar sensing at a passive radar unit.

$\mathcal{A} = \{a_1 \dots a_N\}$ containing integers, the notation $\mathcal{A} + k$ adds integer k to the elements of \mathcal{A} , i.e. $\mathcal{A} + k = \{a_1 + k \dots a_N + k\}$.

II. SYSTEM MODEL

This section introduces the communication-centric ISAC framework considered in this study, in which the downlink transmission from a BS to communication users also serves as an illumination source for passive radar sensing. This system configuration, illustrated in Fig. 1, supports joint sensing and communication functionalities by leveraging transmitted communication signals for environmental sensing.

A. Transmitted Signal Model

The BS is equipped with a uniform linear antenna (ULA) comprising N_t antennas and transmits frames of K_P OFDM symbols over N_P active subcarriers. Each OFDM symbol has a duration $T = \frac{1}{\Delta_f}$, where Δ_f is the subcarrier spacing. To mitigate inter-symbol interference, a cyclic prefix (CP) of duration $T_{CP} = \frac{T}{4}$ is appended to each symbol, resulting in a total symbol duration of $T_o = T + T_{CP}$. The transmitted signal for the k^{th} OFDM symbol within a frame is represented as

$$\mathbf{x}_k(t) = \sum_{n=1}^{N_P} \mathbf{s}_{n,k} c_n(-t) \Pi(t - kT_o), \quad k = 1, \dots, K_P, \quad (1)$$

where $\Pi(t)$ denotes a rectangular window function, $c_n(\tau) = e^{-j2\pi n \Delta_f \tau}$ is the delay response associated with the n^{th} subcarrier, and $\mathbf{s}_{n,k} \in \mathbb{C}^{N_t \times 1}$ represents the modulated symbol on the n^{th} subcarrier for the k^{th} OFDM symbol.

B. Sensing Channel Model

The sensing environment consists of multiple scatterers, including both targets and environmental clutter. Each scatterer is characterized by specific sensing parameters: the AoA θ_m , the AoD ϕ_m , the ToA τ_m , and the Doppler shift $f_{D,m}$. Here, θ_m denotes the AoA from the m^{th} scatterer to the radar unit, while ϕ_m represents the AoD from the BS to the m^{th} scatterer. The parameter τ_m captures the round-trip propagation delay of the waveform transmitted from the BS, scattered by the target, and received at the radar. The associated Doppler shift $f_{D,m}$ arises due to the relative motion of the scatterer.

The channel impulse response (CIR) between the n^{th} BS transmit antenna and the n_r^{th} radar receive antenna is expressed as

$$h_{n_r, n_t}(t, \tau) = \sum_{m=0}^M \alpha_m(t) e^{j2\pi(f_{D,m} + f_{\text{off}})t} a_{n_r}(\theta_m) a_{n_t}(\phi_m) \delta(\tau - \tau_m - \tau_{\text{off}}), \quad (2)$$

where $\delta(\cdot)$ is the Dirac delta function, $\alpha_m(t)$ represents the complex gain for the m^{th} path, and M denotes the total number of scatterers. The terms $a_{n_r}(\theta_m)$ and $a_{n_t}(\phi_m)$ are the receive and transmit steering coefficients, respectively, while τ_{off} and f_{off} represent the timing offset (TO) and frequency offset (FO) due to imperfect synchronization between the BS and radar unit. The spatially separated bistatic configuration, while suitable for ISAC applications, introduces asynchronous clock issues that may impair the sensing accuracy through measurement ambiguities and time-varying phase shifts, limiting coherent processing across time slots [27]. In this study, we assume the BS and radar unit achieve synchronization through a fiber backhaul link connected to a high-accuracy global reference clock. Alternatively, global positioning system (GPS) may be used as a global reference or a reference signal can be generated from the line of sight (LoS) path between the BS and radar unit to estimate and remove TO for localization [28]. Advanced TO/FO compensation techniques, as described in [29]–[31], can further reduce clock instability effects. Under near-perfect synchronization assumptions (i.e., $f_{\text{off}} \approx 0$ and $\tau_{\text{off}} \approx 0$), the CIR from Eq. (2) at the n^{th} subcarrier and k^{th} OFDM symbol is given by

$$\mathbf{H}_{n,k} = \mathbf{A}_r(\Theta) \mathbf{G}_k(\mathbf{f}_D) \mathbf{D}_n(\tau) \mathbf{A}_t^T(\Phi), \in \mathbb{C}^{N_r \times N_t}, \quad (3)$$

where $\mathbf{A}_t(\Phi) = [\mathbf{a}_t(\phi_0) \quad \mathbf{a}_t(\phi_1) \quad \dots \quad \mathbf{a}_t(\phi_M)]$ and $\mathbf{A}_r(\Theta) = [\mathbf{a}_r(\theta_0) \quad \mathbf{a}_r(\theta_1) \quad \dots \quad \mathbf{a}_r(\theta_M)]$ are the transmit and receive steering matrices. The vectors $\mathbf{a}_r(\theta)$ and $\mathbf{a}_t(\phi)$ are the receive and transmit steering vectors, respectively, representing the direction-dependent response of the antenna arrays. For a ULA configuration, they are defined as

$$\begin{aligned} \mathbf{a}_t(\phi) &= e^{-j \frac{2\pi d_t}{\lambda} [0, \dots, N_t - 1]^T \sin(\phi)} \in \mathbb{C}^{N_t \times 1}, \\ \mathbf{a}_r(\theta) &= e^{-j \frac{2\pi d_r}{\lambda} [0, \dots, N_r - 1]^T \sin(\theta)} \in \mathbb{C}^{N_r \times 1}, \end{aligned} \quad (4)$$

where d_t and d_r denote the transmit and receive antenna spacings, respectively, and λ is the signal wavelength. Additionally, $\mathbf{G}_k(\mathbf{f}_D) = \text{diag}([\alpha_0 e^{j2\pi k T_o f_{D,0}} \quad \dots \quad \alpha_M e^{j2\pi k T_o f_{D,M}}])$ includes the complex gains and the phase shifts due to the motion of the scatterers, while $\mathbf{D}_n(\tau) = \text{diag}([c_n(\tau_0) \quad \dots \quad c_n(\tau_M)])$ accounts for the delay responses at the n^{th} subcarrier. In low-mobility scenarios where Doppler shifts are negligible (i.e., $f_{D,m} \approx 0$), the frequency domain CIR from (3) simplifies to

$$\mathbf{H}_n = \mathbf{A}_r(\Theta) \mathbf{G} \mathbf{D}_n(\tau) \mathbf{A}_t^T(\Phi), \quad (5)$$

where the dependence on k and Doppler shifts are omitted, and $\mathbf{G} = \text{diag}([\alpha_0 \quad \dots \quad \alpha_M])$. However, in high-mobility scenarios or at higher frequency bands, the Doppler effect must be considered.

C. Received Signal Model

The radar unit, equipped with a ULA of N_r antennas, receives the downlink OFDM symbols transmitted by the BS. Combining the transmitted signal in (1) with the channel response in (2) and applying fast Fourier transform (FFT), the received signal on the n^{th} subcarrier and k^{th} OFDM symbol is given by

$$\mathbf{y}_{n,k} = \mathbf{H}_{n,k} \mathbf{s}_{n,k} + \mathbf{w}_{n,k} \in \mathbb{C}^{N_r \times 1}, \quad (6)$$

where $\mathbf{H}_{n,k}$ is the bistatic radar channel frequency response for the n^{th} subcarrier and k^{th} OFDM symbol. Here, $\mathbf{w}_{n,k} \in \mathbb{C}^{N_r \times 1}$ is an additive white Gaussian noise (AWGN) vector with zero mean and covariance $\sigma^2 \mathbf{I}$.

D. Channel Estimation

In this work, radar sensing is passively achieved by exploiting the downlink communication signals from the BS without the need for dedicated radar waveforms. This design ensures that the primary communication function of the system remains unaffected, as the full bandwidth is allocated exclusively for communication purposes, thereby avoiding a trade-off between data rates and sensing accuracy. Channel estimation can be performed using both pilot signals and data payloads, which improves efficiency without the need for additional resources. Furthermore, this approach incurs no extra signaling overhead specifically for radar sensing, enabling dual functionality in the existing communication framework.

The proposed methods rely on accurately estimating the radar sensing channel, which encodes key sensing parameters such as AoA, AoD, and ToA. We assume the complex path gains and sensing parameters are time-invariant over a coherent processing interval (CPI), which typically lasts a few milliseconds for environments with moderate-speed targets [5]. Moreover, the radar unit accesses the communication symbols from the BS via a backhaul link connecting the BS and radar unit. Let $\mathbf{S}_n \in \mathbb{C}^{N_t \times K_p}$ represent the matrix of K_p known transmitted OFDM symbols on the n^{th} subcarrier, which are provided to the passive radar via the backhaul connection with the BS [32]. The k^{th} column of \mathbf{S}_n is given by $\mathbf{S}_{n[:,k]} = [\mathbf{s}_{1,k} \ \mathbf{s}_{2,k} \ \cdots \ \mathbf{s}_{N_t,k}]^T$. Similarly, let $\mathbf{Y}_n \in \mathbb{C}^{N_r \times K_p}$ denote the matrix of received symbols $\{\mathbf{y}_{n,k}\}_{k=1}^{K_p}$ on the n^{th} subcarrier. The objective is to estimate the channel response $\mathbf{H}_{n,k}$ using these transmitted and received symbol matrices. For the n^{th} subcarrier, the LS estimator provides a straightforward channel estimate as follows

$$\bar{\mathbf{H}}_n = \mathbf{Y}_n \mathbf{S}_n^H (\mathbf{S}_n \mathbf{S}_n^H)^{-1} = \mathbf{Y}_n \mathbf{S}_n^\dagger, \quad (7)$$

where \mathbf{S}_n^\dagger denotes the Moore-Penrose pseudo-inverse of \mathbf{S}_n , given by $\mathbf{S}_n^\dagger = \mathbf{S}_n^H (\mathbf{S}_n \mathbf{S}_n^H)^{-1}$ for each subcarrier n . The inversion in (7) requires that \mathbf{S}_n have full column rank, which requires $K_p \geq N_t$.

Consider a sequence of sub-frames indexed by p , where each sub-frame comprises $\bar{K}_p \geq N_t$ OFDM symbols. Specifically, the p^{th} sub-frame contains the OFDM symbols indexed by $k = ((p-1)\bar{K}_p + 1), \dots, p\bar{K}_p$. The LS channel estimate for the

n^{th} subcarrier in the p^{th} sub-frame is expressed as

$$\bar{\mathbf{H}}_{n,p} = \mathbf{Y}_{n,p} \mathbf{S}_{n,p}^\dagger, \quad (8)$$

where $\mathbf{Y}_{n,p}$ and $\mathbf{S}_{n,p}$ denote the matrices of received and transmitted symbols, respectively, for the p^{th} sub-frame.

In cases where Doppler shifts are negligible, the estimated channel response on subcarrier n , $\bar{\mathbf{H}}_n$, can be expressed as

$$\begin{aligned} \bar{\mathbf{H}}_n &= \mathbf{Y}_n \mathbf{S}_n^H (\mathbf{S}_n \mathbf{S}_n^H)^{-1} \\ &= (\mathbf{H}_n \mathbf{S}_n + \mathbf{W}_n) \mathbf{S}_n^H (\mathbf{S}_n \mathbf{S}_n^H)^{-1} \\ &= \mathbf{H}_n \mathbf{S}_n \mathbf{S}_n^H (\mathbf{S}_n \mathbf{S}_n^H)^{-1} + \mathbf{W}_n \mathbf{S}_n^H (\mathbf{S}_n \mathbf{S}_n^H)^{-1} \\ &= \mathbf{H}_n + \mathbf{W}_n \mathbf{S}_n^\dagger, \end{aligned} \quad (9)$$

where $\mathbf{W}_n \mathbf{S}_n^\dagger$ represents the noise term induced by the additive noise $\{\mathbf{w}_{n,k}\}_{k=1}^{K_p}$ in the received data. To compile the CSI across all subcarriers, the per-subcarrier estimates $\bar{\mathbf{H}}_n$ are assembled into a single matrix $\bar{\mathbf{H}}$ as follows

$$\begin{aligned} \bar{\mathbf{H}} &= [\text{vec}(\bar{\mathbf{H}}_1) \ \text{vec}(\bar{\mathbf{H}}_2) \ \cdots \ \text{vec}(\bar{\mathbf{H}}_{N_p})] \\ &= \mathbf{H} + \bar{\mathbf{W}}, \end{aligned} \quad (10)$$

where $\bar{\mathbf{H}} \in \mathbb{C}^{N_t N_r \times N_p}$ represents the frequency-domain channel estimates, \mathbf{H} denotes the true CSI, and $\bar{\mathbf{W}}$ is the aggregated noise matrix.

While the LS estimator is computationally efficient, it is sensitive to noise, particularly in low SNR conditions. Alternative approaches, such as the minimum mean squared error (MMSE) estimator, can improve robustness by incorporating prior knowledge of the channel and noise covariance, albeit with a higher computational cost. Regularized LS techniques or hybrid methods may also offer a balanced trade-off between robustness and computational efficiency [33].

III. PROPOSED ALGORITHMS

In this section, we address the problem of sensing parameter estimation within the bistatic communication-centric ISAC framework introduced in Section II. Accurate estimation of the sensing parameters is essential for achieving the dual functionalities of communication and opportunistic sensing. However, standard approaches, such as the MLE, are often computationally prohibitive due to the extensive multi-dimensional optimization required. To provide context, we first present the MLE formulation and discuss its computational limitations. We then introduce two proposed methods, IFFT-C2VNN and PARAMING, which are designed to strike an effective balance between computational efficiency and estimation accuracy.

A. Maximum Likelihood Parameter Estimation

The MLE is widely regarded for its asymptotic efficiency in joint parameter estimation. Nevertheless, it incurs substantial computational costs as it requires a multi-dimensional search over continuous parameter spaces. To jointly estimate AoA, AoD, and ToA parameters, the MLE can be formulated by modeling the observed data as deterministic sequences. Consequently, the joint likelihood function of the observed data \mathcal{Y} , conditioned on known pilot signals \mathcal{S} , noise variance σ^2 , path

gains $\alpha = [\alpha_0, \dots, \alpha_M]$, AoA values Θ , AoD values Φ , and ToA values τ , is given by

$$f(\mathcal{Y}|\mathcal{S}, \sigma^2, \alpha, \Theta, \Phi, \tau) = \prod_{n=1}^{N_p} \prod_{k=1}^{K_p} \frac{1}{\pi \det(\sigma^2 \mathbf{I})} \times \exp \left(-\frac{1}{\sigma^2} \|\mathbf{y}_{n,k} - \mathbf{H}_n(\alpha, \Theta, \Phi, \tau) \mathbf{s}_{n,k}\|^2 \right), \quad (11)$$

where \mathcal{Y} is constructed by stacking the received signal vectors $\mathbf{y}_{n,k} \in \mathbb{C}^{N_r \times 1}$, with its k^{th} column given by $\mathcal{Y}_{[:,k]} = [\mathbf{y}_{1,k} \ \mathbf{y}_{2,k} \ \dots \ \mathbf{y}_{N_p,k}]^T$. Similarly, \mathcal{S} represents the known signals transmitted by the BS, with each column $\mathcal{S}_{[:,k]} = [\mathbf{s}_{1,k} \ \mathbf{s}_{2,k} \ \dots \ \mathbf{s}_{N_p,k}]^T$. Here, $\mathbf{H}_n(\alpha, \Theta, \Phi, \tau)$ denotes the radar channel frequency response for the n^{th} subcarrier, parameterized by the path gains α , angles Θ and Φ , and delays τ . For simplicity, we express the log-likelihood as

$$\mathcal{L} \triangleq \log f(\mathcal{Y}) = g(\sigma^2) - \frac{1}{\sigma^2} \sum_{n=1}^{N_p} \sum_{k=1}^{K_p} \|\mathbf{y}_{n,k} - \mathbf{H}_n \mathbf{s}_{n,k}\|^2,$$

where g is a function of the noise variance σ^2 . Consequently, the MLE criterion can be formulated as

$$\arg \min_{\alpha, \Theta, \Phi, \tau} \left\| \mathcal{Y} - [\mathbf{I}_{N_p} \otimes \mathbf{A}_r(\Theta) \mathbf{G}(\tau) [\mathbf{I}_{N_p} \otimes \mathbf{A}_t^T(\Phi)] \mathcal{S} \right\|^2, \quad (12)$$

where $\mathbf{D}(\tau) = \text{diag}(\mathbf{D}_1(\tau), \dots, \mathbf{D}_{N_p}(\tau))$ represents the delay matrix encoding the ToA information. This estimation problem can be cast as a nonlinear LS optimization over continuous parameter spaces. An exhaustive grid search for MLE estimation in (12) results in a prohibitive computational complexity

$$\mathcal{O}(G_\tau^M G_\theta^M G_\phi^M G_\alpha^{2M} \cdot (N_r N_t M^2 N_p^4 + N_r N_p^3 K_p)), \quad (13)$$

where G_τ , G_θ , G_ϕ , and G_α denote the grid sizes for ToA, AoA, AoD, and path gains, respectively. Here, the terms G_τ^M , G_θ^M , and G_ϕ^M reflect the exponential scaling of complexity with grid points for each parameter across the M paths, while the factors $N_r N_t M^2 N_p^4$ and $N_r N_p^3 K_p$ capture the computation required for each grid point over transmit and receive antennas, subcarriers, and symbols, thereby underscoring the infeasibility of brute-force MLE for real-time applications.

While the search space over the sensing parameters is indeed continuous, a common MLE approach would be to discretize the search space on a uniform grid, which becomes unfeasible for higher number of targets and sensing parameters. Alternatives can be employed such as the space-alternating generalized expectation-maximization (SAGE) algorithm. Specifically, the SAGE algorithm uses alternating expectation-maximization steps, while Richter's MLE (RiMax) leverages gradient-based techniques to explore the likelihood surface. Subspace methods, such as MUSIC and ESPRIT, can further reduce the complexity by exploiting the signal and noise subspaces for parameter estimation, although these methods may experience performance degradation in low SNR scenarios or when scatterers are closely spaced.

In this work, we propose two novel approaches for joint AoA/AoD/ToA estimation: IFFT-C2VNN and PARAMING. IFFT-C2VNN leverages complex-valued convolutional neural networks (CNNs) to directly predict the sensing parameters

from the estimated CSI, providing computational efficiency without compromising estimation accuracy. On the other hand, PARAMING exploits the structured characteristics of the system model, incorporating CSI estimates to achieve an efficient and accurate solution. Both methods are thus designed to deliver high estimation accuracy, while significantly reducing the computational complexity compared to MLE.

B. Deep Learning-based Estimation: IFFT-C2VNN

The IFFT-C2VNN algorithm is a DL architecture tailored for estimating the sensing parameters efficiently from the estimated CSI matrix $\hat{\mathbf{H}}$. In fact, complex-valued CNNs have demonstrated effectiveness in handling multidimensional data [34], making them ideal for radar and signal processing tasks [35], [36]. By leveraging the CSI structure, IFFT-C2VNN provides accurate estimates while addressing the inefficiencies inherent in MLE and subspace-based methods.

1) Input Processing

Given the estimated CSI matrix $\hat{\mathbf{H}}$, as defined in (10), we can decompose it in terms of the sensing parameters as follows

$$\hat{\mathbf{H}} = \mathbf{B}(\Theta, \Phi) \mathbf{G} \mathbf{C}^T(\tau) + \tilde{\mathbf{W}}, \quad (14)$$

where $\mathbf{B}(\Theta, \Phi)$ is the spatial response matrix, defined as

$$\mathbf{B}(\Theta, \Phi) = [\mathbf{a}_t(\phi_0) \otimes \mathbf{a}_r(\theta_0) \ \dots \ \mathbf{a}_t(\phi_M) \otimes \mathbf{a}_r(\theta_M)],$$

and the matrix $\mathbf{C}(\tau) = [\mathbf{c}(\tau_0) \ \dots \ \mathbf{c}(\tau_M)] \in \mathbb{C}^{N_p \times (M+1)}$ encapsulates the ToA information across the subcarriers, while $\tilde{\mathbf{W}}$ represents the overall noise term aggregated across subcarriers and transmit-receive antenna pairs. To process $\hat{\mathbf{H}}$ as input, we first apply an inverse discrete Fourier transform (IDFT) across the subcarrier axis. Let $\mathbf{F} \in \mathbb{C}^{N_p \times N_p}$ denote the discrete Fourier transform (DFT) matrix, with each element of \mathbf{F} defined as

$$[\mathbf{F}]_{n,k} = \frac{1}{\sqrt{N_p}} e^{-j \frac{2\pi}{N_p} nk}, \quad n, k = 0, 1, \dots, N_p - 1. \quad (15)$$

The transformation applied to the transpose of $\hat{\mathbf{H}}$ yields

$$\mathbf{F}^H \hat{\mathbf{H}}^T = \mathbf{F}^H \mathbf{C}(\tau) \mathbf{G} \mathbf{B}^T(\Theta, \Phi) + \mathbf{F}^H \tilde{\mathbf{W}}. \quad (16)$$

To further examine $\mathbf{F}^H \mathbf{C}(\tau)$, we apply an IDFT to each column of the delay matrix $\mathbf{C}(\tau)$. The (p, m) -th entry of the resulting matrix $\mathbf{F}^H \mathbf{C}(\tau)$ is given by

$$\begin{aligned} [\mathbf{F}^H \mathbf{C}(\tau)]_{p,m} &= \frac{1}{\sqrt{N_p}} \sum_{n=0}^{N_p-1} e^{j \frac{2\pi}{N_p} pn} e^{-j 2\pi n \Delta_f \tau_m} \\ &= \frac{1}{\sqrt{N_p}} \sum_{n=0}^{N_p-1} e^{j 2\pi n (\frac{p}{N_p} - \Delta_f \tau_m)}. \end{aligned} \quad (17)$$

For non-fractional delays, where each delay τ_m aligns with an integer multiple of the sampling interval $\Delta_t = \frac{1}{N_p \Delta_f}$, the term $\frac{p}{N_p} - \Delta_f \tau_m$ becomes an integer for certain indices p . In this case, if $\tau_m = \frac{k}{N_p \Delta_f}$ for an integer k , we have

$$[\mathbf{F}^H \mathbf{C}(\tau)]_{p,m} = \begin{cases} \sqrt{N_p}, & p = k, \\ 0, & \text{otherwise.} \end{cases} \quad (18)$$

The resulting sparsity in $\mathbf{F}^H \mathbf{C}(\tau)$, with non-zero entries only at rows corresponding to each discrete delay τ_m , allows each target's delay to occupy a distinct row in $\mathbf{F}^H \mathbf{C}(\tau)$, facilitating a straightforward extraction of the individual target

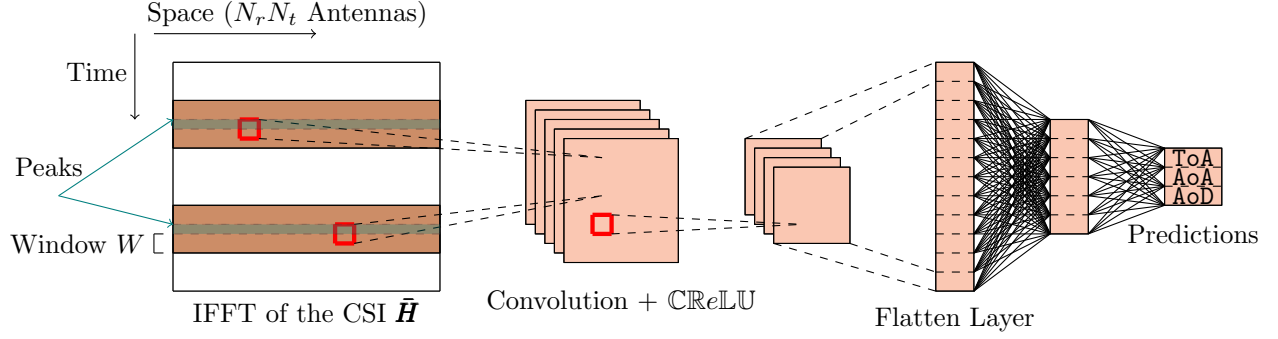


Fig. 2: Architecture of the IFFT-C2VNN algorithm, consisting of complex-valued convolutional layers and CReLU activation functions.

parameters. This structured sparsity is preserved in $\mathbf{F}^H \bar{\mathbf{H}}^T$ under non-fractional delay assumptions, where each delay τ_m corresponds to a unique row index $\hat{i}_m = N_p \Delta_f \tau_m$. Consequently, $\mathbf{F}^H \bar{\mathbf{H}}^T$ exhibits non-zero entries only in rows indexed by $\{\hat{i}_1, \dots, \hat{i}_M\}$, with other rows containing near-zero values. This structured sparsity greatly simplifies the parameter estimation by isolating each target's delay contribution, thus supporting efficient extraction of individual sensing parameters.

In the general case with fractional delays, where τ_m is not an integer multiple of the sampling interval Δ_t , $\frac{P}{N_p} - \Delta_f \tau_m$ is generally non-integer. This causes each delay's contribution to spread across multiple rows in $\mathbf{F}^H \mathbf{C}(\tau)$ and produces a less sparse structure in $\mathbf{F}^H \bar{\mathbf{H}}^T$. Here, each delay's influence is represented by a sinc-like spread, with energy dispersed over multiple rows, generating phase variations across a range of rows. To manage this, we apply a windowed input representation centered around the peak row for each target's primary delay index, forming an input tensor $\bar{\mathcal{I}}_m \in \mathbb{C}^{(2W+1) \times N_r N_t}$ for the m^{th} target, as defined by

$$\bar{\mathcal{I}}_m = \begin{bmatrix} \bar{h}_{[\hat{i}_m - W], 1} & \cdots & \bar{h}_{[\hat{i}_m - W], N_r N_t} \\ \vdots & \ddots & \vdots \\ \bar{h}_{[\hat{i}_m], 1} & \cdots & \bar{h}_{[\hat{i}_m], N_r N_t} \\ \vdots & \ddots & \vdots \\ \bar{h}_{[\hat{i}_m + W], 1} & \cdots & \bar{h}_{[\hat{i}_m + W], N_r N_t} \end{bmatrix}, \quad (19)$$

where $\bar{h}_{[p], j}$ denotes the p^{th} row and j^{th} column entry in $\mathbf{F}^H \bar{\mathbf{H}}^T$. The window of size $(2W+1)$ effectively isolates each target's delay contributions, enabling the NN to capture fractional delay information from the phase variations in the local neighborhood and accurately estimate the sensing parameters.

It is crucial to note that the current approach assumes resolvable scatterers, where each peak corresponds to a distinct scatterer. However, in cases of non-resolvability, where multiple scatterers contribute to a single peak, a preliminary classification step is required to estimate the number of paths within each peak. In such cases, non-resolvability is typically mitigated in the angular domain, as it is highly improbable for

two targets to be sufficiently close in space to produce identical AoA, AoD, and delay combinations. This classification guarantees that the fixed-size NN output aligns with the expected number of parameters to estimate, thereby ensuring a reliable sensing performance.

2) Network Architecture

The IFFT-C2VNN architecture, illustrated in Fig. 2, is designed to process the windowed input representations $\bar{\mathcal{I}}_m$ for each target, facilitating the efficient estimation of the ToA, AoA, and AoD parameters. The network structure includes two complex-valued convolutional layers, each followed by a CReLU activation function, and concludes with two complex linear layers that output the estimated sensing parameters. Each convolutional layer comprises 10 complex filters, with the n^{th} filter defined as $\mathbf{W}_n = \mathbf{W}_n^r + j\mathbf{W}_n^i$. For a complex input $\mathbf{z} = \mathbf{x} + j\mathbf{y}$, where \mathbf{x} and \mathbf{y} denote the real and imaginary parts, respectively, the resulting feature map $\hat{\mathbf{z}}$ from the convolutional layer is computed as

$$\hat{\mathbf{z}} = (\mathbf{W}_n^r * \mathbf{x} - \mathbf{W}_n^i * \mathbf{y}) + j(\mathbf{W}_n^r * \mathbf{y} + \mathbf{W}_n^i * \mathbf{x}). \quad (20)$$

The complex-valued linear layers follow a similar structure, with weights and biases represented as $\mathbf{W} = \mathbf{W}^r + j\mathbf{W}^i$ and $\mathbf{b} = \mathbf{b}^r + j\mathbf{b}^i$, respectively. Given an input $\mathbf{z} = \mathbf{x} + j\mathbf{y}$, the output $\hat{\mathbf{z}}$ of the linear layer is calculated as

$$\hat{\mathbf{z}} = (\mathbf{W}^r \mathbf{x} - \mathbf{W}^i \mathbf{y} + \mathbf{b}^r) + j(\mathbf{W}^r \mathbf{y} + \mathbf{W}^i \mathbf{x} + \mathbf{b}^i). \quad (21)$$

The CReLU activation function introduces non-linearity, enabling the network to effectively model complex-domain non-linear functions. This function is defined as

$$\text{CReLU}(\hat{\mathbf{z}}) = \text{ReLU}(\Re(\hat{\mathbf{z}})) + j \text{ReLU}(\Im(\hat{\mathbf{z}})), \quad (22)$$

where $\text{ReLU}(x) = \max(0, x)$.

3) Training Procedure and Hyperparameters

The network is trained using a synthetic dataset comprising E simulations, i.e. training points, generated in accordance with the system model outlined in Section II. In each simulation, M targets are randomly positioned within the environment. The training objective is to minimize the MSE between

the predicted and true parameters, as defined by

$$L_{\text{MSE}} = \frac{1}{ME} \sum_{e=1}^E \sum_{m=1}^M \left[\left(\hat{\theta}_m^{\text{tar}}(e) - \theta_m(e) \right)^2 + \left(\hat{\phi}_m^{\text{tar}}(e) - \phi_m(e) \right)^2 + \left(\hat{\tau}_m^{\text{tar}}(e) - \tau_m(e) \right)^2 \right], \quad (23)$$

where $\hat{\theta}_m^{\text{tar}}(e)$, $\hat{\phi}_m^{\text{tar}}(e)$, and $\hat{\tau}_m^{\text{tar}}(e)$ represent the predicted AoA, AoD, and ToA for the m^{th} target in the e^{th} training point, respectively.

C. PARAMING

The PARAMING algorithm offers an efficient method for extracting the joint AoA, AoD, and ToA parameters from the CSI matrix $\bar{\mathbf{H}}$. In contrast to traditional MLE or subspace-based methods, which rely on exhaustive grid searches or complex multi-dimensional optimizations, PARAMING capitalizes on a structured decomposition of $\bar{\mathbf{H}}$ into sub-array and subcarrier blocks, allowing for an efficient parameter extraction through matrix transformations. Below, we present the matrix construction, parameterization, and algorithmic steps for isolating the sensing parameters.

Given an estimate of the CSI $\bar{\mathbf{H}}$, PARAMING introduces sub-array sizes $1 < M_t \leq N_t$ and $1 < M_r \leq N_r$ along with a sub-OFDM symbol size $1 < M_p \leq N_p$ subcarriers. Then, by leveraging the Vandermonde structure of the transmit/receive ULA configurations and the regular subcarrier spacing, a Hankel-block-Hankel-block-Hankel type matrix can be formed using the entries of $\bar{\mathbf{H}}$ as follows

$$\bar{\mathbf{H}} = \begin{bmatrix} \bar{\mathbf{H}}_1 & \bar{\mathbf{H}}_2 & \dots & \bar{\mathbf{H}}_{K_t} \\ \bar{\mathbf{H}}_2 & \bar{\mathbf{H}}_3 & \dots & \bar{\mathbf{H}}_{K_t+1} \\ \vdots & \vdots & \ddots & \vdots \\ \bar{\mathbf{H}}_{M_t} & \bar{\mathbf{H}}_{M_t+1} & \dots & \bar{\mathbf{H}}_{N_t} \end{bmatrix}, \quad (24)$$

where $K_t \triangleq N_t - M_t + 1$ denotes the number of transmit sub-arrays. Each block $\bar{\mathbf{H}}_i$ itself has a Hankel-block structure given by

$$\bar{\mathbf{H}}_i = \begin{bmatrix} \bar{\mathbf{H}}_{i,1} & \bar{\mathbf{H}}_{i,2} & \dots & \bar{\mathbf{H}}_{i,K_N} \\ \bar{\mathbf{H}}_{i,2} & \bar{\mathbf{H}}_{i,3} & \dots & \bar{\mathbf{H}}_{i,K_N+1} \\ \vdots & \vdots & \ddots & \vdots \\ \bar{\mathbf{H}}_{i,M_p} & \bar{\mathbf{H}}_{i,M_p+1} & \dots & \bar{\mathbf{H}}_{i,N_p} \end{bmatrix}, \quad (25)$$

where $K_N \triangleq N_p - M_p + 1$ represents the number of sub-OFDM frames, and each entry $\bar{\mathbf{H}}_{i,j}$ is itself a Hankel matrix formed from the CSI entries as

$$\bar{\mathbf{H}}_{i,j} = \begin{bmatrix} \bar{h}_{i,j,1} & \bar{h}_{i,j,2} & \dots & \bar{h}_{i,j,K_r} \\ \bar{h}_{i,j,2} & \bar{h}_{i,j,3} & \dots & \bar{h}_{i,j,K_r+1} \\ \vdots & \vdots & \ddots & \vdots \\ \bar{h}_{i,j,M_r} & \bar{h}_{i,j,M_r+1} & \dots & \bar{h}_{i,j,N_r} \end{bmatrix}, \quad (26)$$

where $K_r \triangleq N_r - M_r + 1$ is the number of receive sub-arrays. Each element $\bar{h}_{i,j,k}$ corresponds to an entry in $\bar{\mathbf{H}}$ as defined in (10), with a compact indexing notation $\bar{h}_{i,j,k} = \bar{\mathbf{H}}_{[k+(i-1)N_r,j]}$. Using this structured representation, we express $\bar{\mathbf{H}}$ in terms of the ToA, AoA, and AoD parameters

$$\bar{\mathbf{H}} = \mathcal{B}_{M_r, M_p, M_t}(\Theta, \Phi, \tau) \mathcal{G} \mathcal{B}_{K_r, K_N, K_t}^T(\Theta, \Phi, \tau) + \bar{\mathbf{W}}, \quad (27)$$

where \mathcal{G} is the path gain matrix, $\bar{\mathbf{W}}$ represents noise, while the manifold $\mathcal{B}_{n,m,p}(\Theta, \Phi, \tau)$ is defined as

$$\mathcal{B}_{n,m,p}(\Theta, \Phi, \tau) = \begin{bmatrix} \mathbf{A}_r(\Theta)_{[1:n,:]} \\ \vdots \\ \mathbf{A}_r(\Theta)_{[1:n,:]} \mathbf{D}_\tau^{m-1}(\tau) \\ \mathbf{A}_r(\Theta)_{[1:n,:]} \mathbf{D}_\tau(\tau) \mathbf{D}_\phi(\Phi) \\ \vdots \\ \mathbf{A}_r(\Theta)_{[1:n,:]} \mathbf{D}_\tau^{m-1}(\tau) \mathbf{D}_\phi(\Phi) \\ \vdots \\ \mathbf{A}_r(\Theta)_{[1:n,:]} \mathbf{D}_\tau(\tau) \mathbf{D}_\phi^{p-1}(\Phi) \\ \vdots \\ \mathbf{A}_r(\Theta)_{[1:n,:]} \mathbf{D}_\tau^{m-1}(\tau) \mathbf{D}_\phi^{p-1}(\Phi) \end{bmatrix}, \quad (28)$$

where $\mathbf{D}_\tau(\tau) = \text{diag}([\mathbf{c}(\tau_1) \dots \mathbf{c}(\tau_M)])$ and $\mathbf{D}_\phi(\Phi) = \text{diag}([\mathbf{a}(\phi_1) \dots \mathbf{a}(\phi_M)])$. Then, we control the sub-array sizes to inflate the left/right manifold $\mathcal{B}_{M_r, M_p, M_t}$ containing the ToA, AoA and AoD information. To exploit this, we form two interconnected matrices from $\bar{\mathbf{H}}$ as follows

$$\bar{\mathbf{H}}^{(1)} \triangleq \bar{\mathbf{H}}_{[:, \mathcal{S}^{(1)}]} = \mathcal{B}_{M_r, M_p, M_t}(\Theta, \Phi, \tau) \mathbf{G} \mathbf{\Pi}^T + \bar{\mathbf{W}}^{(1)}, \quad (29)$$

and

$$\bar{\mathbf{H}}^{(2)} \triangleq \bar{\mathbf{H}}_{[:, \mathcal{S}^{(2)}]} = \mathcal{B}_{M_r, M_p, M_t}(\Theta, \Phi, \tau) \mathbf{G} \mathbf{D}_\tau(\tau) \mathbf{\Pi}^T + \bar{\mathbf{W}}^{(2)}, \quad (30)$$

where $\mathcal{S}^{(1)} = \bigcup_{k=0}^{K_t-1} \{\mathcal{S} + kK_rK_N\}$ and $\mathcal{S}^{(2)} = \mathcal{S}^{(1)} + K_r$ are sets of selected column indices from $\bar{\mathbf{H}}$, given $\mathcal{S} = \{1, 2, \dots, K_r(K_N - 1)\}$. Here, $\mathbf{\Pi} = [\mathcal{B}_{K_r, K_N, K_t}]_{[\mathcal{S}^{(1)}, :]}$, while $\bar{\mathbf{W}}^{(1)}$ and $\bar{\mathbf{W}}^{(2)}$ are noise matrices with elements from $\bar{\mathbf{W}}$. Subsequently, the matrices $\bar{\mathbf{H}}^{(1)}$ and $\bar{\mathbf{H}}^{(2)}$ are exploited to estimate the ToAs via the combination

$$\bar{\mathbf{H}}_\gamma \triangleq \bar{\mathbf{H}}^{(2)} - \gamma \bar{\mathbf{H}}^{(1)} = \mathcal{B}_{M_r, M_p, M_t}(\Theta, \Phi, \tau) \mathbf{G} (\mathbf{D}_\tau(\tau) - \gamma \mathbf{I}) \mathbf{\Pi}^T + \bar{\mathbf{W}}_\gamma, \quad (31)$$

where $\bar{\mathbf{W}}_\gamma = \bar{\mathbf{W}}^{(2)} - \gamma \bar{\mathbf{W}}^{(1)}$. Given that $\mathbf{\Pi}$ and $\mathcal{B}_{M_r, M_p, M_t}(\Theta, \Phi, \tau)$ are full-rank matrices, the rank of $\bar{\mathbf{H}}_\gamma$ decreases at $\gamma = \mathbf{c}_1(\tau_m)$ for each m . Thus, we can estimate the ToAs by performing a grid search over τ and testing the M^{th} largest singular value of $\bar{\mathbf{H}}_\gamma$, then we choose the M minima of the resulting spectrum. Alternatively, since the aforementioned procedure is highly complex, we resort to a truncated SVD method. In essence, we first perform a classical SVD on $\bar{\mathbf{H}}^{(1)}$, namely $\bar{\mathbf{H}}^{(1)} = \mathbf{U} \mathbf{\Sigma} \mathbf{V}^H$, where \mathbf{U} and \mathbf{V} represent the left and right singular vectors of $\bar{\mathbf{H}}^{(1)}$, respectively. Moreover, $\mathbf{\Sigma}$ is composed of the singular values of $\bar{\mathbf{H}}^{(1)}$ along its diagonal in decreasing order. After this SVD, we perform a truncation by first obtaining a diagonal $M \times M$ matrix $\bar{\mathbf{\Sigma}}$ consisting of the strongest M singular values in $\mathbf{\Sigma}$. The corresponding left and right singular vectors are stacked in $\bar{\mathbf{U}}$ and $\bar{\mathbf{V}}$, respectively. Then, we compute

$$\mathbf{T} = \bar{\mathbf{\Sigma}}^{-1} \bar{\mathbf{U}}^H \bar{\mathbf{H}}^{(2)} \bar{\mathbf{V}}, \quad (32)$$

whose eigenvalues are represented by $\gamma_1 \dots \gamma_M$. Note that these eigenvalues are estimates of $\mathbf{c}_1(\hat{\tau}_m)$. Hence, a simple

approach to compute $\{\hat{\tau}_m\}_{m=1}^M$ is via

$$\hat{\tau}_m = -\frac{\angle \gamma_m}{2\pi\Delta_f}, \quad \forall m = 1 \dots M. \quad (33)$$

To obtain the AoDs/AoAs that are associated with each of the estimated ToAs. We perform an LS fit based on the received signal

$$\hat{\mathbf{Y}} = \arg \min_{\mathbf{Y}} \|\bar{\mathbf{H}} - \mathbf{Y}\mathbf{C}^T(\hat{\boldsymbol{\tau}})\|^2 = \bar{\mathbf{H}}\mathbf{C}^*(\hat{\boldsymbol{\tau}})(\mathbf{C}^T(\hat{\boldsymbol{\tau}})\mathbf{C}^*(\hat{\boldsymbol{\tau}}))^{-1}. \quad (34)$$

Note that $\hat{\mathbf{Y}}$ is indeed an LS estimate of $\mathbf{B}(\boldsymbol{\Theta}, \boldsymbol{\Phi})\mathbf{G}$, given the ToAs. Based on this, we perform a second LS stage tailored for estimating the $\mathbf{B}(\boldsymbol{\Theta}, \boldsymbol{\Phi})$ as such

$$\{\hat{\mathbf{B}}, \hat{\boldsymbol{\alpha}}\} = \begin{cases} \arg \min_{\mathbf{B}, \boldsymbol{\alpha}} \|\hat{\mathbf{Y}} - \mathbf{B}\mathbf{G}\|^2, \\ \text{subject to } \|\mathbf{B}_{[:,m]}\| = 1, \mathbf{G} = \text{diag}(\boldsymbol{\alpha}). \end{cases} \quad (35)$$

Then, we separate the optimization problem in (35) into M independent problems due to the diagonal structure of \mathbf{G} , i.e.

$$\hat{\mathbf{B}}_{[:,m]} = \begin{cases} \arg \min_{\mathbf{b}_m} \|\hat{\mathbf{Y}}_{[:,m]} - \alpha_m \mathbf{b}_m\|^2, \\ \text{subject to } \|\mathbf{b}_m\| = 1, \end{cases} \quad (36)$$

where the solution is trivial and is given as

$$\hat{\mathbf{b}}_m = \frac{\hat{\mathbf{Y}}_{[:,m]}}{\|\hat{\mathbf{Y}}_{[:,m]}\|}, \quad \forall m = 1 \dots M \quad (37)$$

and $|\hat{\alpha}_m| = \frac{\|\hat{\mathbf{Y}}_{[:,m]}\|}{\sqrt{N_t N_r}}$. Now, given $\{\hat{\mathbf{b}}_m\}_{m=1}^M$, we simultaneously estimate the AoAs and AoDs using a 2D regression on the phases of $\{\hat{\mathbf{b}}_m\}_{m=1}^M$ via the following problem

$$(\hat{\theta}_m, \hat{\phi}_m, \hat{\delta}_m) = \arg \min_{\theta_m, \phi_m, \delta_m} \left\| \angle \hat{\mathbf{b}}_m - \Xi \begin{bmatrix} \theta_m \\ \phi_m \\ \delta_m \end{bmatrix} \right\|^2 = \Xi^\dagger \angle \hat{\mathbf{b}}_m, \quad (38)$$

for all m , where $\Xi = [\mathbf{1}_{N_t} \otimes \mathbf{e}_{N_r}, \mathbf{e}_{N_t} \otimes \mathbf{1}_{N_r}, \mathbf{1}_{N_t N_r}] \in \mathbb{C}^{N_t N_r \times 3}$ and δ_m includes the phase offset that is contained within α_m . In order to avoid abrupt phase changes, the phases of $\angle \hat{\mathbf{b}}_m$ have to be unwrapped. A summary of the proposed sensing method is given in **Algorithm 1**.

D. Extension to Doppler estimation

As discussed in Section II, high-mobility scenarios induce Doppler shifts that manifest as time-dependent phase changes in the received signals. Therefore, accurately estimating these shifts is essential for determining the velocities of potential targets. Let $\mathbf{G}_k(\mathbf{f}_D)$ be defined as in Eq. (3), incorporating both Doppler effects and path gains. Indeed, the methods must process the temporal evolution of the channel over multiple OFDM symbols to incorporate Doppler estimation. Specifically, this requires estimating the channel over a series of sub-frames to capture the Doppler-induced phase shifts across time. For the PARAMING algorithm, this adaptation allows for Doppler estimation with minimal structural changes. However, it necessitates operating over a sequence of sub-frames and ensuring that these sub-frames lie within a CPI, where Doppler shifts influence the channel's temporal variation, but the channel remains stable enough for coherent processing. Let $\bar{\mathbf{H}}_{n,p}$ denote the LS channel estimate for the n^{th} subcarrier in the p^{th} sub-frame, as defined in (8). By constructing the

Algorithm 1 PARAMING (joint ToA/AoA/AoD Estimation)

- 1: INPUT: $\{\mathbf{Y}_n\}_{n=1}^{N_p}, \{\mathbf{S}_n\}_{n=1}^{N_p}$
CHANNEL ESTIMATION:
 - 2: Obtain $\{\hat{\mathbf{H}}_n\}_{n=1}^{N_p}$ according to equation (7)
 - SENSING ESTIMATION:
 - 3: Arrange $\hat{\mathbf{H}}$ as given by equations (24) and (25).
 - 4: Compute $\hat{\mathbf{H}}^{(1)}, \hat{\mathbf{H}}^{(2)}$ as (29) and (30), respectively.
 - 5: Get a truncated SVD of $\hat{\mathbf{H}}^{(1)}$.
 $[\bar{\mathbf{U}}, \bar{\boldsymbol{\Sigma}}, \bar{\mathbf{V}}] \leftarrow \text{TSVD}_M(\hat{\mathbf{H}}^{(1)}).$
 - 6: Calculate \mathbf{T} via (32), given $\bar{\mathbf{U}}, \bar{\boldsymbol{\Sigma}}, \bar{\mathbf{V}}, \hat{\mathbf{H}}^{(1)}$.
 - 7: Get the eigenvalues of \mathbf{T} , i.e. $\{\sigma_m\}_{m=1}^M$.
 - 8: Estimate $\hat{\tau}_m$ given σ_m via (33). Repeat for $m = 1 \dots M$.
 - 9: Obtain $\hat{\mathbf{Y}}$ through equation (34).
 - 10: Given $\hat{\mathbf{Y}}$, obtain $\{\hat{\mathbf{b}}_m\}_{m=1}^M$ via (37).
 - 11: For each m , obtain (θ_m, ϕ_m) as discussed in (38).
 - 12: **return** $(\hat{\tau}_1, \hat{\theta}_1, \hat{\phi}_1) \dots (\hat{\tau}_M, \hat{\theta}_M, \hat{\phi}_M)$.
-

matrices from (24) through (26) and applying the PARAMING algorithm, the phase offsets for each target in the p^{th} sub-frame, denoted as $\{\hat{\delta}_m^p\}_{m=1}^M$, can be estimated according to (38). Notably, the Hankel-block-Hankel-block-Hankel structure used for AoA, AoD, and ToA estimation remains applicable. The temporal evolution of the phase offsets within $\mathbf{G}_k(\mathbf{f}_D)$ now embeds the Doppler shift information. Assuming the estimation is conducted over \tilde{K}_p sub-frames, let $\{\hat{\delta}_m^p\}_{p=1}^{\tilde{K}_p}$ denote the estimated phase offsets for the m^{th} target. These phase offsets can be expressed as

$$\hat{\delta}_m^p = \delta_m^0 + 2\pi p K_p T_0 f_{D,m} + \tilde{\epsilon}_{m,p}, \quad (39)$$

where δ_m^0 represents the initial phase offset, $f_{D,m}$ is the Doppler shift of the m^{th} target, and $\tilde{\epsilon}_{m,p}$ denotes the phase estimation error. Since the phase evolves linearly with time in the presence of Doppler shifts, a simple 2D regression on the estimated phase offsets suffices to extract the Doppler frequencies of all targets.

Similarly, extending the IFFT-C2VNN algorithm to estimate Doppler frequencies requires processing the temporal evolution of the channel. The extension involves stacking the estimated CSIs from multiple sub-frames to incorporate the temporal progression into the model's input. The addition of this temporal dimension enables the network to learn Doppler-induced phase variations alongside the spatial and delay parameters. To achieve this, the input to the NN is modified to include \tilde{K}_p sub-frames, resulting in a 3D input tensor. This modification necessitates the use of 3D complex-valued convolutional layers instead of the 2D layers employed previously, enabling the model to extract spatio-temporal features that encode the Doppler frequency information. The temporal convolution captures the inter-frame phase progression induced by Doppler, while the spatial convolution continues to process spatial and frequency-domain information. Moreover, the architecture is further adapted by modifying the output layer to account for the additional Doppler frequency parameters.

Specifically, the output layer now provides four outputs per target, corresponding to the AoA, AoD, ToA, and Doppler frequency. To ensure robust performance, the training process involves generating datasets that span various Doppler shift scenarios, along with diverse SNR conditions. This training strategy enables the model to generalize effectively across a wide range of operational settings.

IV. COMPUTATIONAL COMPLEXITY

In this section, we comprehensively analyze the computational complexity of both IFFT-C2VNN and PARAMING, quantifying it by the total number of additions and multiplications required for estimating the sensing parameters.

We begin by outlining the primary computational sub-blocks that significantly contribute to the complexity of PARAMING:

- SVD of $\hat{\mathcal{H}}^{(1)}$ using the Golub–Reinsch algorithm [37].
- Computation of \mathbf{T} , as defined in (32), involving matrix multiplications among $\bar{\mathbf{V}} \in \mathbb{C}^{K_t K_r (K_{N_p} - 1) \times M}$, $\bar{\mathbf{U}}^H \in \mathbb{C}^{M \times M_r M_t M_p}$, and the diagonal matrix $\bar{\mathbf{\Sigma}}^{-1} \in \mathbb{C}^{M \times M}$.
- Eigenvalue decomposition of $\mathbf{T} \in \mathbb{C}^{M \times M}$, using a QZ decomposition as \mathbf{T} has no specific structure.
- Calculation of ToAs using (33) via a coordinate rotation digital computer (CORDIC) algorithm, which provides phase estimates of the eigenvalues.
- Estimation of $\hat{\mathbf{Y}}$ as per (34), followed by a 2D regression to estimate AoAs and AoDs as described in (38).

The computational complexity details of these sub-blocks are omitted due to lack of space. However, summing them yields the following total computational cost for PARAMING

$$\begin{aligned}
 T_{\text{add}} &= 9K_{\text{trp}}^3 + 8M_{\text{tr}}K_{\text{trp}}^2 + 4M_{\text{tr}}^2K_{\text{trp}} + M^3 \\
 &\quad + M^2(M_{\text{tr}} + 4N_{\text{cord}} + 2N_p - 4) \\
 &\quad + M[M_{\text{tr}}(K_{\text{trp}} - 1) - 2N_{\text{cord}} + N_t N_r (N_p + 2) \\
 &\quad - N_p + 4], \\
 T_{\text{mul}} &= 9K_{\text{trp}}^3 + 8M_{\text{tr}}K_{\text{trp}}^2 + 4M_{\text{tr}}^2K_{\text{trp}} + M^3 \\
 &\quad + M^2(M_{\text{tr}} + 2N_p + 3) \\
 &\quad + M[M_{\text{tr}}K_{\text{trp}} + N_t N_r (N_p + 3) + 9]. \quad (40)
 \end{aligned}$$

where T_{add} and T_{mul} denote the total number of additions and multiplications, respectively. Here, $M_{\text{tr}} = M_t M_r M_p$, $K_{\text{trp}} = K_t K_r (K_{N_p} - 1)$, and N_{cord} is the number of iterations for the CORDIC algorithm.

For IFFT-C2VNN, the computational complexity is measured by counting the total operations within the architecture using the FLOPS profiler in TensorFlow [38]. As outlined in Section III-B, we explore multiple window configurations around target peaks to reduce the computational cost. To provide a benchmark, we also present the computational complexity of the grid-based MLE method, as defined in (13). For comparability, we assume $G_\alpha = 1$, simulating a scenario where the path gain α is known to the MLE. We set $G_\phi = G_\theta = 180$, yielding a grid resolution of approximately 1° for AoA and AoD within a search range of -90° to 90° . For ToA, we assign

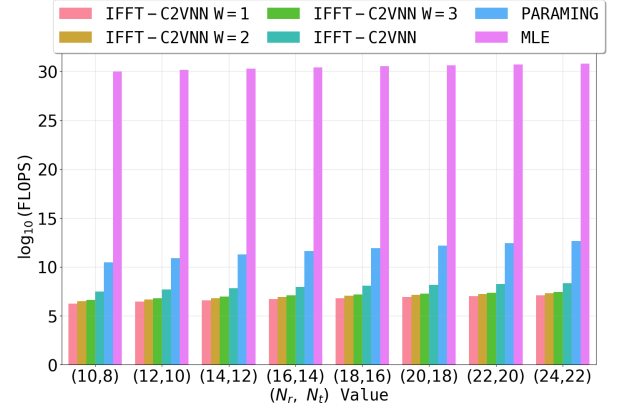


Fig. 3: Computational complexity analysis in terms of floating point operations per second (FLOPS) for IFFT-C2VNN with its variants (W) and PARAMING.

$G_r = 128$, which corresponds to a precision gain of 2 beyond initial coarse estimates.

In Fig. 3, we present the computational complexity as a function of the number of transmit and receive antennas (N_r, N_t) in a scenario with three targets. The results clearly show that the MLE requires significantly more operations, with approximately 10^{22} times the operations of IFFT-C2VNN and 10^{19} times more than PARAMING. Moreover, PARAMING generally incurs a higher complexity than the various configurations of IFFT-C2VNN. Notably, as the system scale increases, the complexity of PARAMING escalates more rapidly than that of IFFT-C2VNN, highlighting the latter's suitability for resource-constrained scenarios.

In addition to the inference complexity, we evaluate the training complexity of IFFT-C2VNN, focusing on the computational cost of forward and backward passes over multiple epochs. In complex-valued networks, each convolutional operation entails additional arithmetic due to the simultaneous processing of real and imaginary components. For a network input $\mathcal{H}_{\text{in}}^1 \in \mathbb{C}^{(2W+1) \times N_r N_t}$, where W denotes the window size, each convolutional layer $l = 1, \dots, L$ comprises C_l complex filters $\mathbf{f}_l^{c_l} \in \mathbb{C}^{h_f^l \times w_f^l}$ with stride S_l and padding P_l . The input and output dimensions at each layer are $\mathcal{H}_{\text{in}}^l \in \mathbb{C}^{h^l \times w^l \times C_{l-1}}$ and $\mathcal{H}_{\text{out}}^l \in \mathbb{C}^{h_{\text{out}}^l \times w_{\text{out}}^l \times C_l}$, where

$$h_{\text{out}}^l = \frac{h^l + 2P_l - h_f^l}{S_l} + 1, \quad w_{\text{out}}^l = \frac{w^l + 2P_l - w_f^l}{S_l} + 1. \quad (41)$$

The forward pass complexity per layer is

$$C_{\text{forward}} = \mathcal{O} \left(\sum_{l=1}^L 4 h_{\text{out}}^l w_{\text{out}}^l C_{l-1} h_f^l w_f^l C_l \right), \quad (42)$$

where the factor of 4 accounts for real and imaginary components in complex-valued convolutions.

The backward pass, approximately twice as computationally intensive as the forward pass, includes error propagation, gradient calculation, and weight updates. With \mathcal{E} epochs and

TABLE I: Simulation Parameters

Parameter	Value
Number of transmit antennas (N_t)	8 [41], [42]
Number of receive antennas (N_r)	10 [41]
Carrier frequency (f_c)	28 GHz [42]
Antenna spacing ($d_r = d_t = \lambda/2$)	0.53 cm
Number of subcarriers (N_p)	64 [43]
Number of OFDM symbols per sub-frame (K_p)	10 [43]
Number of sub-frames (\tilde{K}_p)	4 [44]
Subcarrier spacing (Δ_f)	960 kHz [45]
OFDM symbol duration (T_o)	1.3 μ s
Temporal resolution ($\Delta_t = \frac{1}{N_p \Delta_f}$)	16.27 ns

dataset size \mathcal{B} , the total training complexity is

$$C_{\text{training}} = \mathcal{O} \left(\sum_{l=1}^L 12 \mathcal{E} \mathcal{B} h_{\text{out}}^l w_{\text{out}}^l C_{l-1} h_f^l w_f^l C_l \right). \quad (43)$$

It is important to note that this computational cost applies only during the training phase. For inference, only the forward pass is required, as defined in (42), making real-time applications feasible with suitable hardware and software optimizations.

V. NUMERICAL EVALUATION

In this section, we present a comprehensive performance evaluation of the proposed PARAMING and IFFT-C2VNN algorithms, alongside a comparison with state-of-the-art estimation methods, including Bartlett, MUSIC, Root-MUSIC, and deterministic maximum likelihood (DML) [39], [40]. These methods represent well-established baselines for parameter estimation and were specifically adapted to our communication-centric ISAC context. By incorporating these methods into our analysis, we aim to highlight the comparative advantages of the proposed approaches under varied noise conditions. The simulation setup adheres to realistic ISAC system configurations, as summarized in Table I. The CIR model used in our simulations, as defined in Eq. (2), accounts for the superposition of reflections from multiple scatterers, including both targets and environmental clutter. A refined classification of scatterers, achieved by estimating the sensing parameters across multiple coherence time intervals or employing advanced ML techniques, can enhance the distinction between these entities by enabling the identification of scatterer dynamics and facilitating the discrimination between static clutter and moving targets.

For the benchmarked grid-based methods, namely Bartlett, MUSIC, and DML, predefined search grids were employed to estimate the sensing parameters. To balance estimation accuracy and computational feasibility, the grid resolution was set to 0.05° for AoA and AoD, and $\Delta_t/5$ for ToA. These resolutions ensure fair comparisons with the proposed methods while keeping computational complexity manageable. Additionally, the Cramér-Rao bound (CRB), which serves as the theoretical performance bound, is discussed in **Appendix A**. For the PARAMING method, the sub-array dimensions were set to $M_t = \lfloor \frac{N_t}{2} \rfloor$, $M_r = \lfloor \frac{N_r}{2} \rfloor$, and the sub-OFDM symbol dimension to $M_p = \lfloor \frac{N_p}{2} \rfloor$.

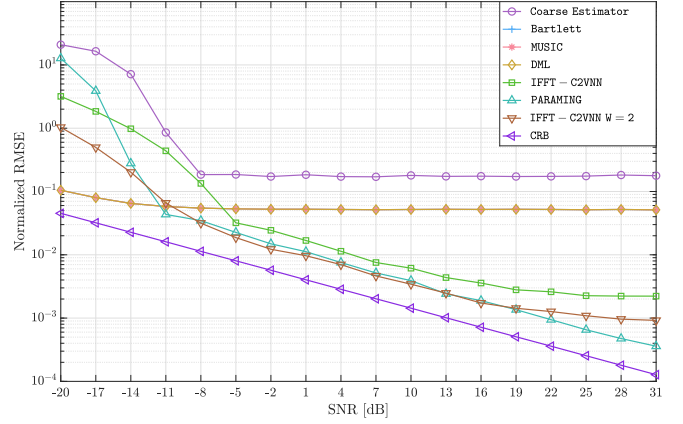
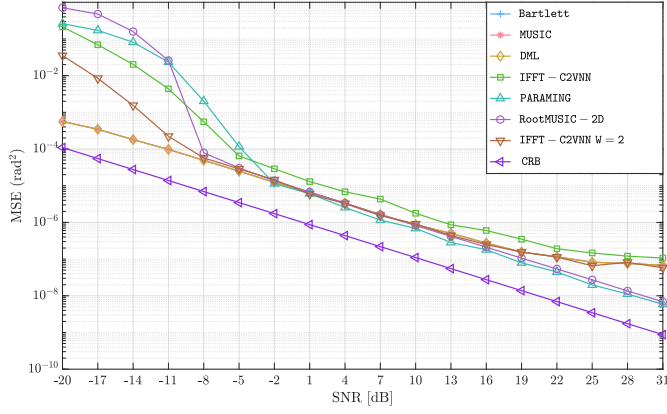


Fig. 4: Normalized root mean squared error (RMSE) of ToA estimation for the proposed methods and benchmarked approaches, compared against the CRB.

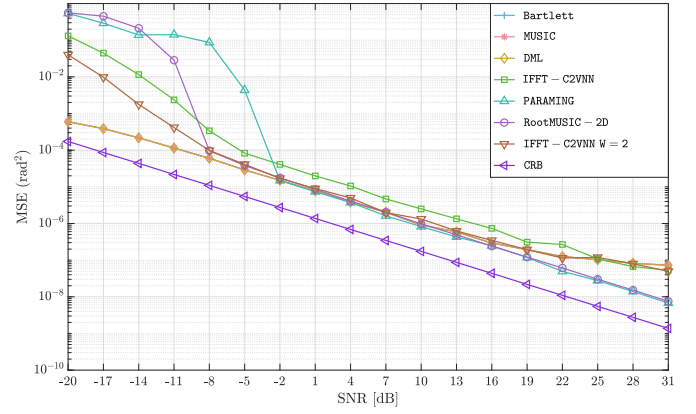
To address the question of optimal training strategies for IFFT-C2VNN in simulations with varying SNR levels, we evaluated two approaches: training separate models at fixed SNR levels (e.g., -5 dB) versus a single model trained on data spanning a wide range of SNR values (-5 to 40 dB). Notably, the results reveal that the latter approach significantly enhances the model's generalization ability and robustness across noise conditions while obviating the need for SNR-specific models. The IFFT-C2VNN model was trained using the Adam optimizer with a learning rate of 10^{-4} , a batch size of 128, over 300 epochs. Moreover, a variant of IFFT-C2VNN with $W = 2$ was evaluated to assess the impact of restricting the input CSI to peak regions, effectively reducing noise and improving model convergence. Monte Carlo experiments were conducted with independently generated channel realizations, random scatterer positions, and SNR levels spanning -20 to 31 dB.

Figure 4 illustrates the ToA estimation performance in terms of RMSE normalized by the system's temporal resolution Δ_t . Among the benchmarked grid-based methods, Bartlett, MUSIC, and DML exhibit identical performance under the considered single-target scenario due to their similar derivations. Their accuracy stagnates at higher SNR values due to the predefined grid resolution $\Delta_t/5$, which limits further improvement. Indeed, while finer grids could improve accuracy, they would result in prohibitive computational complexity and compromise fairness in comparison with the proposed methods. Conversely, the proposed methods, PARAMING and IFFT-C2VNN, demonstrate superior performance, estimating effectively across both low and high SNR levels. PARAMING achieves the closest alignment to the CRB at high SNR, reflecting its enhanced precision. IFFT-C2VNN, trained over a broad SNR range, exhibits strong robustness, while its $W = 2$ variant further improves accuracy by focusing on peak regions of the CSI input.

The performance comparison for AoA and AoD estimation is presented in Fig. 5, highlighting the MSE across the same range of SNR levels. Similar to the ToA case, Bartlett, MUSIC,



(a) AoA estimation performance.



(b) AoD estimation performance.

Fig. 5: Comparison of AoA and AoD estimation performance in terms of MSE across SNR levels.

TABLE II: Execution time of the proposed and benchmarked methods.

Category	Method	Execution Time (s)
Proposed Methods	IFFT-C2VNN	0.06
	PARAMING	0.26
Benchmarked Methods	Bartlett	96.85
	MUSIC	104.07
	RootMUSIC-2D	38.81
	DML	95.61

and DML exhibit nearly identical performance performance, constrained by the 0.05° grid resolution. RootMUSIC-2D, despite only estimating AoA and AoD and leveraging data from all subcarriers, achieves reasonable performance but does not surpass PARAMING. Nevertheless, it demonstrates an earlier waterfall region, providing an advantage in low-SNR scenarios. Finally, PARAMING achieves the closest alignment to the CRB, while IFFT-C2VNN shows strong robustness but stagnates at very high SNR levels. The $W = 2$ variant of IFFT-C2VNN further improves accuracy, reinforcing the effectiveness of the proposed methods for sensing parameter estimation. When compared to the CRB, all compared methods, including both proposed methods, exhibit sub-optimal performance across all sensing parameters. For instance, in the case of ToA estimation, achieving a normalized RMSE of 10^{-2} requires an SNR approximately 9 dB higher than the CRB. A similar performance gap is observed for the AoA and AoD estimations, as shown in Fig. 5.

To evaluate the computational efficiency, we measured the execution times of the proposed and benchmarked methods on an high-performance computing (HPC) cluster equipped with AMD EPYC 7742 64-Core Processors operating at 2.25 GHz. Each node consists of 128 CPU cores and 480 GB of memory; however, the jobs were executed on nodes specifically configured with 32 GB of memory to simulate realistic computational constraints. Table II summarizes the latency results, averaged over 300 Monte Carlo trials.

Among the compared methods, IFFT-C2VNN achieves the

lowest latency of **0.06** seconds, followed by PARAMING at **0.26** seconds. These results underscore the computational efficiency of the proposed methods, with latencies remaining well within the acceptable range for real-time ISAC applications, particularly when leveraging hardware accelerators such as graphics processing units (GPUs) or field programmable gate arrays (FPGAs). By contrast, the grid-based benchmarked methods exhibit significantly higher latencies due to their reliance on exhaustive grid searches over fine-grained grids, which impose a substantial computational burden. Furthermore, these methods necessitate large dictionaries of steering vectors, thereby introducing scalability challenges and considerable space complexity. Notably, the computational intractability of DML with multiple targets necessitated limiting the analysis to the single-target case to ensure feasible execution. Additionally, the limitations imposed by the predefined grid resolution remain applicable in multi-target scenarios, leading to similar conclusions regarding their performance. RootMUSIC-2D, which estimates only AoA and AoD, achieves a substantially lower latency compared to other grid-based methods. However, its latency still far exceeds that of the proposed methods. Moreover, extending RootMUSIC to a 3D variant for simultaneous AoA, AoD, and ToA estimation proves computationally infeasible due to the exponential increase in complexity associated with higher-dimensional polynomial-based estimation. In summary, the proposed methods not only achieve superior estimation accuracy but also significantly outperform the benchmarked methods in terms of latency, thus demonstrating their suitability for efficient and scalable communication-centric ISAC applications.

In addition to the joint estimation of AoA, AoD, and ToA, we extended the proposed PARAMING and IFFT-C2VNN methods to include Doppler frequency estimation, as detailed in Section III-D. Simulations were conducted to evaluate their performance, considering target velocities uniformly distributed up to 30 m s^{-1} , corresponding to Doppler shifts of up to $\pm 2.8 \text{ kHz}$. The Doppler estimation performance, measured

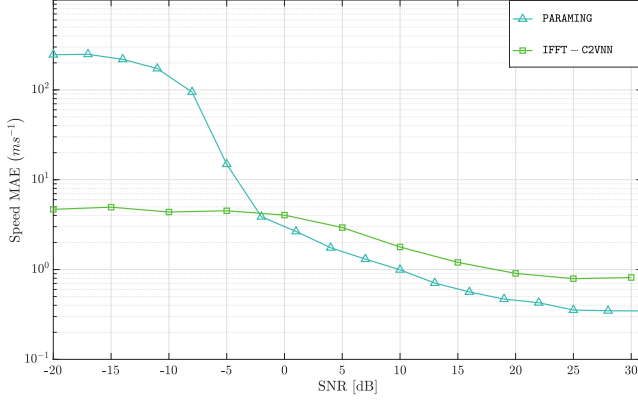


Fig. 6: Performance of the proposed methods for speed estimation, measured in MAE.

in terms of mean absolute error (MAE), is presented in Fig. 6. The results demonstrate that both methods reliably estimate Doppler frequencies, with PARAMING achieving superior accuracy at high SNR levels. Specifically, PARAMING attains an MAE as low as 0.3 m s^{-1} , compared to 0.8 m s^{-1} for IFFT-C2VNN. These findings reaffirm the potential of both methods for high-resolution sensing parameter estimation.

VI. CONCLUSION

In this paper, we have introduced two novel approaches, IFFT-C2VNN and PARAMING and, for joint sensing parameter estimation in a communication-centric bistatic ISAC configuration, where a passive radar leverages the downlink communication signals from an existing infrastructure to estimate the sensing parameters for multiple targets in the environment. PARAMING employs a parameterized approach that integrates system-specific characteristics, such as array geometries, to extract the sensing parameters from a Hankel matrix derived from the estimated CSI. In contrast, the IFFT-C2VNN employs a DL-based convolutional architecture to process the estimated channel matrix for parameter estimation.

Performance results underscore the effectiveness of the proposed methods in enhancing the sensing capabilities within communication-centric ISAC systems while also reducing the computational complexity. Future research directions include extending the estimation framework to fully capture the multidimensional aspect of the sensing problem by incorporating both azimuth and elevation angles, ToAs, Doppler shifts, and the fully polarimetric complex path weights. This extension should also consider realistic factors such as local scattering, path loss, synchronization offsets, and cross-polarization effects to ensure robustness and adaptability in diverse scenarios.

APPENDIX A

CRAMÉR-RAO BOUND EXPRESSIONS

The Fisher information matrix (FIM) is given as follows

$$\mathbf{F} \triangleq \mathbb{E} \left[\frac{\partial \mathcal{L}(\boldsymbol{\xi})}{\partial \boldsymbol{\xi}} \frac{\partial \mathcal{L}(\boldsymbol{\xi})}{\partial \boldsymbol{\xi}}^T \right], \quad (44)$$

where $\boldsymbol{\xi}$ is the vector of unknown parameters, namely $\boldsymbol{\xi} = [\sigma \ \boldsymbol{\Theta} \ \boldsymbol{\Phi} \ \boldsymbol{\tau} \ \bar{\boldsymbol{\alpha}}]$, where $\bar{\boldsymbol{\alpha}}$ represents the real-part of $\boldsymbol{\alpha}$ and

$\tilde{\boldsymbol{\alpha}}$ represents the imaginary-part of $\boldsymbol{\alpha}$. Furthermore, $\mathcal{L}(\boldsymbol{\xi})$ is the log-likelihood of the model, i.e. $\mathcal{L}(\boldsymbol{\xi}) = \log f(\mathbf{Y})$ and $f(\mathbf{Y})$ is the probability density function (PDF) of the observed data defined in (11). The FIM is partitioned according to the unknown variables, i.e. for any two parameter quantities, $\mathbf{F}_{\mathbf{a},\mathbf{b}} = \mathbb{E} \left[\frac{\partial \mathcal{L}(\boldsymbol{\xi})}{\partial \mathbf{a}} \frac{\partial \mathcal{L}(\boldsymbol{\xi})}{\partial \mathbf{b}}^T \right]$. Note that it is easy to see $\mathbf{F}_{\sigma,\sigma} = \frac{N_r N_p K_p}{\sigma^4}$ and $\mathbf{F}_{\sigma,\boldsymbol{\Theta}} = \mathbf{F}_{\sigma,\boldsymbol{\Phi}} = \mathbf{F}_{\sigma,\boldsymbol{\tau}} = \mathbf{F}_{\sigma,\bar{\boldsymbol{\alpha}}} = \mathbf{F}_{\sigma,\tilde{\boldsymbol{\alpha}}} = \mathbf{0}^T$. Now, denoting $\boldsymbol{\Xi}_i = \mathbf{a}_r(\theta_i) \mathbf{a}_t^T(\phi_i)$, $\boldsymbol{\Xi}_i^r = \mathbf{d}_r(\theta_i) \mathbf{a}_t^T(\phi_i)$ and $\boldsymbol{\Xi}_i^t = \mathbf{a}_r(\theta_i) \mathbf{d}_t^T(\phi_i)$, where $\mathbf{d}_r(\theta) = \frac{\partial \mathbf{a}_r(\theta)}{\partial \theta}$ and $\mathbf{d}_t(\phi) = \frac{\partial \mathbf{a}_t(\phi)}{\partial \phi}$ are the partial derivatives of the receive and transmit steering vectors with respect to θ and ϕ , respectively. To this end, we summarize the FIM block-matrices appearing in (44) as follows. First, we compute all second-order partial derivatives whenever $\boldsymbol{\Theta}$ appears, i.e.

$$[\mathbf{F}_{\boldsymbol{\Theta},\boldsymbol{\Theta}}]_{i,j} = \frac{2}{\sigma^2} \sum_{n,k} \Re \left(\mathbf{s}_{n,k}^H [\alpha_i c_n(\tau_i) \boldsymbol{\Xi}_i^r]^H [\alpha_j c_n(\tau_j) \boldsymbol{\Xi}_j^r] \mathbf{s}_{n,k} \right),$$

$$[\mathbf{F}_{\boldsymbol{\Theta},\boldsymbol{\Phi}}]_{i,j} = \frac{2}{\sigma^2} \sum_{n,k} \Re \left(\mathbf{s}_{n,k}^H [\alpha_i c_n(\tau_i) \boldsymbol{\Xi}_i^r]^H [\alpha_j c_n(\tau_j) \boldsymbol{\Xi}_j^t] \mathbf{s}_{n,k} \right),$$

$$[\mathbf{F}_{\boldsymbol{\Theta},\boldsymbol{\tau}}]_{i,j} = \frac{2}{\sigma^2} \sum_{n,k} \Re \left(\mathbf{s}_{n,k}^H [\alpha_i c_n(\tau_i) \boldsymbol{\Xi}_i^r]^H [\alpha_j d_n(\tau_j) \boldsymbol{\Xi}_j] \mathbf{s}_{n,k} \right),$$

$$[\mathbf{F}_{\boldsymbol{\Theta},\bar{\boldsymbol{\alpha}}}]_{i,j} = \frac{2}{\sigma^2} \sum_{n,k} \Re \left(\mathbf{s}_{n,k}^H [\alpha_i c_n(\tau_i) \boldsymbol{\Xi}_i^r]^H [c_n(\tau_j) \boldsymbol{\Xi}_j] \mathbf{s}_{n,k} \right),$$

$$[\mathbf{F}_{\boldsymbol{\Theta},\tilde{\boldsymbol{\alpha}}}]_{i,j} = \frac{2}{\sigma^2} \sum_{n,k} \Re \left(\mathbf{s}_{n,k}^H [\alpha_i c_n(\tau_i) \boldsymbol{\Xi}_i^r]^H [j c_n(\tau_j) \boldsymbol{\Xi}_j] \mathbf{s}_{n,k} \right),$$

where $d_n(\tau) = \frac{\partial c_n(\tau)}{\partial \tau}$. Then, we compute all second-order partial derivatives whenever $\boldsymbol{\Phi}$ appears, i.e.

$$[\mathbf{F}_{\boldsymbol{\Phi},\boldsymbol{\Phi}}]_{i,j} = \frac{2}{\sigma^2} \sum_{n,k} \Re \left(\mathbf{s}_{n,k}^H [\alpha_i c_n(\tau_i) \boldsymbol{\Xi}_i^t]^H [\alpha_j c_n(\tau_j) \boldsymbol{\Xi}_j^t] \mathbf{s}_{n,k} \right),$$

$$[\mathbf{F}_{\boldsymbol{\Phi},\boldsymbol{\tau}}]_{i,j} = \frac{2}{\sigma^2} \sum_{n,k} \Re \left(\mathbf{s}_{n,k}^H [\alpha_i c_n(\tau_i) \boldsymbol{\Xi}_i^t]^H [\alpha_j d_n(\tau_j) \boldsymbol{\Xi}_j] \mathbf{s}_{n,k} \right),$$

$$[\mathbf{F}_{\boldsymbol{\Phi},\bar{\boldsymbol{\alpha}}}]_{i,j} = \frac{2}{\sigma^2} \sum_{n,k} \Re \left(\mathbf{s}_{n,k}^H [\alpha_i c_n(\tau_i) \boldsymbol{\Xi}_i^t]^H [c_n(\tau_j) \boldsymbol{\Xi}_j] \mathbf{s}_{n,k} \right),$$

$$[\mathbf{F}_{\boldsymbol{\Phi},\tilde{\boldsymbol{\alpha}}}]_{i,j} = \frac{2}{\sigma^2} \sum_{n,k} \Re \left(\mathbf{s}_{n,k}^H [\alpha_i c_n(\tau_i) \boldsymbol{\Xi}_i^t]^H [j c_n(\tau_j) \boldsymbol{\Xi}_j] \mathbf{s}_{n,k} \right),$$

Following the above expressions, we compute all FIM partial derivatives where $\boldsymbol{\tau}$ appears

$$[\mathbf{F}_{\boldsymbol{\tau},\boldsymbol{\tau}}]_{i,j} = \frac{2}{\sigma^2} \sum_{n,k} \Re \left(\mathbf{s}_{n,k}^H [\alpha_i d_n(\tau_i) \boldsymbol{\Xi}_i]^H [\alpha_j d_n(\tau_j) \boldsymbol{\Xi}_j] \mathbf{s}_{n,k} \right),$$

$$[\mathbf{F}_{\boldsymbol{\tau},\bar{\boldsymbol{\alpha}}}]_{i,j} = \frac{2}{\sigma^2} \sum_{n,k} \Re \left(\mathbf{s}_{n,k}^H [\alpha_i d_n(\tau_i) \boldsymbol{\Xi}_i]^H [c_n(\tau_j) \boldsymbol{\Xi}_j] \mathbf{s}_{n,k} \right),$$

$$[\mathbf{F}_{\boldsymbol{\tau},\tilde{\boldsymbol{\alpha}}}]_{i,j} = \frac{2}{\sigma^2} \sum_{n,k} \Re \left(\mathbf{s}_{n,k}^H [\alpha_i d_n(\tau_i) \boldsymbol{\Xi}_i]^H [j c_n(\tau_j) \boldsymbol{\Xi}_j] \mathbf{s}_{n,k} \right),$$

Next, we compute all partial derivatives where $\bar{\boldsymbol{\alpha}}$ appears

$$[\mathbf{F}_{\bar{\boldsymbol{\alpha}},\bar{\boldsymbol{\alpha}}}]_{i,j} = \frac{2}{\sigma^2} \sum_{n,k} \Re \left(\mathbf{s}_{n,k}^H [c_n(\tau_i) \boldsymbol{\Xi}_i]^H [c_n(\tau_j) \boldsymbol{\Xi}_j] \mathbf{s}_{n,k} \right),$$

$$[\mathbf{F}_{\bar{\boldsymbol{\alpha}},\tilde{\boldsymbol{\alpha}}}]_{i,j} = \frac{2}{\sigma^2} \sum_{n,k} \Re \left(\mathbf{s}_{n,k}^H [c_n(\tau_i) \boldsymbol{\Xi}_i]^H [j c_n(\tau_j) \boldsymbol{\Xi}_j] \mathbf{s}_{n,k} \right),$$

Then we compute all partial derivatives where $\tilde{\boldsymbol{\alpha}}$ appears

$$[\mathbf{F}_{\tilde{\boldsymbol{\alpha}},\tilde{\boldsymbol{\alpha}}}]_{i,j} = \frac{2}{\sigma^2} \sum_{n,k} \Re \left(\mathbf{s}_{n,k}^H [j c_n(\tau_i) \boldsymbol{\Xi}_i]^H [j c_n(\tau_j) \boldsymbol{\Xi}_j] \mathbf{s}_{n,k} \right).$$

Now, the CRB for the parameters of interest (i.e. AoA, AoD, ToA) is obtained as follows

$$\begin{aligned} \text{CRB}(\boldsymbol{\Theta}) &= [\mathbf{F}^{-1}]_{2:(M+1),2:(M+1)} \\ \text{CRB}(\boldsymbol{\Phi}) &= [\mathbf{F}^{-1}]_{(M+2):(2M+1),(M+2):(2M+1)} \\ \text{CRB}(\boldsymbol{\tau}) &= [\mathbf{F}^{-1}]_{(2M+2):(3M+1),(2M+2):(3M+1)} \end{aligned} \quad (45)$$

REFERENCES

- [1] F. Liu *et al.*, "Integrated sensing and communications: Toward dual-functional wireless networks for 6G and beyond," *IEEE J. Sel. Areas Commun.*, vol. 40, no. 6, pp. 1728–1767, 2022.
- [2] A. Bazzi and M. Chafii, "On outage-based beamforming design for dual-functional radar-communication 6G systems," *IEEE Trans. Wireless Commun.*, vol. 22, no. 8, pp. 5598–5612, 2023.
- [3] Q. Qi, X. Chen, C. Zhong, and Z. Zhang, "Integrated sensing, computation and communication in B5G cellular internet of things," *IEEE Trans. Wireless Commun.*, vol. 20, no. 1, pp. 332–344, 2021.
- [4] M. Chafii, L. Bariah, S. Muhaidat, and M. Debbah, "Twelve scientific challenges for 6G: Rethinking the foundations of communications theory," *IEEE Commun. Surv. Tutor.*, 2023.
- [5] J. A. Zhang *et al.*, "An overview of signal processing techniques for joint communication and radar sensing," *IEEE J. Sel. Topics Signal Process.*, vol. 15, no. 6, pp. 1295–1315, 2021.
- [6] C. Ouyang, Y. Liu, and H. Yang, "MIMO-ISAC: Performance analysis and rate region characterization," *IEEE Wirel. Commun. Lett.*, vol. 12, no. 4, pp. 669–673, 2023.
- [7] A. Hassanien, M. G. Amin, Y. D. Zhang, and F. Ahmad, "Signaling strategies for dual-function radar communications: an overview," *IEEE Trans. Aerosp. Electron. Syst.*, vol. 31, no. 10, pp. 36–45, 2016.
- [8] F. Liu, L. Zhou, C. Masouros, A. Li, W. Luo, and A. Petropulu, "Toward dual-functional radar-communication systems: Optimal waveform design," *IEEE Trans. Signal Process.*, vol. 66, no. 16, pp. 4264–4279, 2018.
- [9] S. K. Dehkordi, J. C. Hauffe, P. Jung, and G. Caire, "Hierarchical soft-thresholding for parameter estimation in beam-space OTFS integrated sensing and communication," in *ICC 2023 - IEEE International Conference on Communications*, pp. 2939–2945, 2023.
- [10] W. Xu, Y. Xiao, A. Liu, M. Lei, and M.-J. Zhao, "Joint scattering environment sensing and channel estimation based on non-stationary markov random field," *IEEE Trans. Wireless Commun.*, vol. 23, no. 5, pp. 3903–3917, 2024.
- [11] L. Pucci, E. Matricardi, E. Paolini, W. Xu, and A. Giorgetti, "Performance analysis of a bistatic joint sensing and communication system," in *2022 IEEE International Conference on Communications Workshops (ICC Workshops)*, pp. 73–78, 2022.
- [12] J. Zhao, Z. Lu, J. A. Zhang, S. Dong, and S. Zhou, "Multiple-target doppler frequency estimation in ISAC with clock asynchronism," *IEEE Trans. Veh. Technol.*, vol. 73, no. 1, pp. 1382–1387, 2024.
- [13] S. Naoumi, A. Bazzi, R. Bomfin, and M. Chafii, "Complex neural network based joint AoA and AoD estimation for bistatic ISAC," *IEEE J. Sel. Topics Signal Process.*, pp. 1–15, 2024.
- [14] Y. Wu, F. Lemic, C. Han, and Z. Chen, "Sensing integrated DFT-spread OFDM waveform and deep learning-powered receiver design for terahertz integrated sensing and communication systems," *IEEE Trans. Commun.*, vol. 71, no. 1, pp. 595–610, 2023.
- [15] R. Bomfin and M. Chafii, "Unique word-based frame design for bistatic integrated sensing and communication," *IEEE Trans. Wireless Commun.*, vol. 23, no. 12, pp. 19333–19349, 2024.
- [16] A. Zhang, M. L. Rahman, X. Huang, Y. J. Guo, S. Chen, and R. W. Heath, "Perceptive mobile networks: Cellular networks with radio vision via joint communication and radar sensing," *IEEE Veh. Technol. Mag.*, vol. 16, no. 2, pp. 20–30, 2021.
- [17] M. L. Rahman, J. A. Zhang, X. Huang, Y. J. Guo, and R. W. Heath, "Framework for a perceptive mobile network using joint communication and radar sensing," *IEEE Trans. Aerosp. Electron. Syst.*, vol. 56, no. 3, pp. 1926–1941, 2020.
- [18] Y. Liu, G. Liao, Y. Chen, J. Xu, and Y. Yin, "Super-resolution range and velocity estimations with OFDM integrated radar and communications waveform," *IEEE Trans. Veh. Technol.*, vol. 69, no. 10, pp. 11659–11672, 2020.
- [19] Y. Xiang, Y. Gao, X. Yang, S. Kang, and M. Shao, "An ESPRIT-based moving target sensing method for MIMO-OFDM ISAC systems," *IEEE Commun. Lett.*, vol. 27, no. 12, pp. 3205–3209, 2023.
- [20] Z. Gao, Z. Wan, D. Zheng, S. Tan, C. Masouros, D. W. K. Ng, and S. Chen, "Integrated sensing and communication with mmWave massive MIMO: A compressed sampling perspective," *IEEE Trans. Wireless Commun.*, vol. 22, no. 3, pp. 1745–1762, 2023.
- [21] X. Li, J. A. Zhang, K. Wu, Y. Cui, and X. Jing, "CSI-ratio-based doppler frequency estimation in integrated sensing and communications," *IEEE Sensors Journal*, vol. 22, no. 21, pp. 20886–20895, 2022.
- [22] Z.-M. Liu, C. Zhang, and P. S. Yu, "Direction-of-arrival estimation based on deep neural networks with robustness to array imperfections," *IEEE Trans. Antennas Propag.*, vol. 66, no. 12, pp. 7315–7327, 2018.
- [23] J. Fuchs, R. Weigel, and M. Gardill, "Single-snapshot direction-of-arrival estimation of multiple targets using a multi-layer perceptron," in *2019 IEEE MTT-S International Conference on Microwaves for Intelligent Mobility (ICMIM)*, pp. 1–4, 2019.
- [24] J. Fuchs, M. Gardill, M. Lübke, A. Dubey, and F. Lurz, "A machine learning perspective on automotive radar direction of arrival estimation," *IEEE Access*, vol. 10, pp. 6775–6797, 2022.
- [25] Z. Zhang, Q. Chang, J. Xing, and L. Chen, "Deep-learning methods for integrated sensing and communication in vehicular networks," *Veh. Commun.*, vol. 40, p. 100574, 2023.
- [26] J. Hu, I. Valiulahi, and C. Masouros, "ISAC receiver design: A learning-based two-stage joint data-and-target parameter estimation," *IEEE Wirel. Commun. Lett.*, vol. 13, no. 8, pp. 2105–2109, 2024.
- [27] J. A. Zhang, K. Wu, X. Huang, Y. J. Guo, D. Zhang, and R. W. Heath, "Integration of radar sensing into communications with asynchronous transceivers," *IEEE Commun. Mag.*, vol. 60, no. 11, pp. 106–112, 2022.
- [28] H. Kuschel, D. Cristallini, and K. E. Olsen, "Tutorial: Passive radar tutorial," *IEEE Aerosp. Electron. Syst. Mag.*, vol. 34, no. 2, pp. 2–19, 2019.
- [29] X. Chen, Z. Feng, J. A. Zhang, X. Yuan, and P. Zhang, "Kalman filter-based sensing in communication systems with clock asynchronism," *IEEE Trans. Commun.*, 2023.
- [30] J. Pegoraro, J. O. Lacruz, T. Azzino, M. Mezzavilla, M. Rossi, J. Widmer, and S. Rangan, "JUMP: Joint communication and sensing with unsynchronized transceivers made practical," *IEEE Trans. Wireless Commun.*, vol. 23, no. 8, pp. 9759–9775, 2024.
- [31] Z. Ni, J. A. Zhang, X. Huang, K. Yang, and J. Yuan, "Uplink sensing in perceptive mobile networks with asynchronous transceivers," *IEEE Trans. Signal Process.*, vol. 69, pp. 1287–1300, 2021.
- [32] A. Bazzi and M. Chafii, "Low dynamic range for RIS-aided bistatic integrated sensing and communication," 2024.
- [33] P. Sure and C. M. Bhuma, "A survey on OFDM channel estimation techniques based on denoising strategies," *Eng. Sci. Technol. Int. J.*, vol. 20, no. 2, pp. 629–636, 2017.
- [34] C. Trabelsi *et al.*, "Deep complex networks," *arXiv preprint*, 2017. arXiv:1705.09792.
- [35] G. K. Papageorgiou, M. Sellathurai, and Y. C. Eldar, "Deep networks for direction-of-arrival estimation in low SNR," *IEEE Trans. Signal Process.*, vol. 69, pp. 3714–3729, 2021.
- [36] J. Bassey, L. Qian, and X. Li, "A survey of complex-valued neural networks," *arXiv preprint*, 2021. arXiv:2101.12249.
- [37] R. C. Ward, "The combination shift QZ algorithm," *SIAM J. Numer. Anal.*, vol. 12, no. 6, pp. 835–853, 1975.
- [38] M. Abadi *et al.*, "TensorFlow: A system for large-scale machine learning," in *OSDI*, vol. 16, pp. 265–283, 2016.
- [39] B. Rao and K. Hari, "Performance analysis of Root-Music," *IEEE Trans. Acoust., Speech, Signal Process.*, vol. 37, no. 12, pp. 1939–1949, 1989.
- [40] P. Häcker and B. Yang, "Single snapshot DOA estimation," *Adv. Radio Sci.*, vol. 8, pp. 251–256, 2010.
- [41] K. Hou and S. Zhang, "Secure integrated sensing and communication exploiting target location distribution," in *GLOBECOM 2023 - 2023 IEEE Global Communications Conference*, pp. 4933–4938, 2023.
- [42] W. Chen, X. Lin, J. Lee, A. Toskala, S. Sun, C. F. Chiasserini, and L. Liu, "5G-advanced toward 6G: Past, present, and future," *IEEE J. Sel. Areas Commun.*, vol. 41, no. 6, pp. 1592–1619, 2023.
- [43] P. Jiang, T. Wang, B. Han, X. Gao, J. Zhang, C.-K. Wen, S. Jin, and G. Y. Li, "AI-aided online adaptive OFDM receiver: Design and experimental results," *IEEE Trans. Wireless Commun.*, vol. 20, no. 11, pp. 7655–7668, 2021.
- [44] F. E. H. Germany and A. C. France, "5G waveform candidate selection," 2021.
- [45] J. Choi, H. Jang, and K. W. Choi, "Phase noise compensation techniques for arbitrary reference signal configurations in mmWave and Sub-THz bands," *IEEE Wirel. Commun. Lett.*, vol. 13, no. 3, pp. 597–601, 2024.